Available online at www.sciencedirect.com
SCIENCE DIRECT®
Ultramicroscopy 106 (2006) 466–474
ultramicroscopy
www.elsevier.com/locate/ultramic

Contact mechanics and tip shape in AFM-based nanomechanical measurements

Malgorzata Kopycinska-Müller*, Roy H. Geiss, Donna C. Hurley

Materials Reliability Division, National Institute of Standards and Technology, Boulder, CO 80305-3328, USA

Received 12 September 2005; received in revised form 30 November 2005; accepted 15 December 2005

Abstract

Stiffness–load curves obtained in quantitative atomic force acoustic microscopy (AFAM) measurements depend on both the elastic properties of the sample and the geometry of the atomic force microscope (AFM) tip. The geometry of silicon AFM tips changes when used in contact mode, affecting measurement accuracy. To study the influence of tip geometry, we subjected ten AFM tips to the same series of AFAM measurements. Changes in tip shape were observed in the scanning electron microscope (SEM) between individual AFAM tests. Because all of the AFAM measurements were performed on the same sample, variations in AFAM stiffness–load curves were attributed to differences in tip geometry. Contact-mechanics models that assumed simple tip geometries were used to analyze the AFAM data, but the calculated values for tip dimensions did not agree with those provided by SEM images. Therefore, we used a power-law approach that allows for a nonspherical tip geometry. We found that after several AFAM measurements, the geometry of the tips at the very end is intermediate between those of a flat punch and a hemisphere. These results indicate that the nanoscale tip-sample contact cannot easily be described in terms of simple, ideal geometries.
© 2006 Elsevier B.V. All rights reserved.

Keywords: Atomic force microscopy (AFM); Contact mechanics; Elastic modulus; Tip characterization

1. Introduction

The atomic force microscope (AFM) has been used in a variety of methods to image material properties with unprecedented spatial resolution. Because AFM images are usually qualitative, the efforts of many groups are currently focused on improving the quantitative capability of these techniques. Our own interests target quantitative measurements of nanoscale elastic properties. The AFM appears ideally suited for this due to its scanning capabilities, the small diameter of the sensor tip (~10–100 nm), and the ability to apply very small static loads (~0.1–5 μN).

For the most part, AFM-based methods that promise elastic-property information are dynamic approaches in which the AFM cantilever is vibrated at or near its resonant frequencies [1–3]. Several of these techniques are labeled "acoustic" or "ultrasonic" methods, due to the characteristic frequency range (~0.1–3 MHz) applied to the AFM cantilever during measurement. Included in this category are ultrasonic force microscopy [4], heterodyne force microscopy [5], ultrasonic atomic force microscopy [6], and atomic force acoustic microscopy (AFAM) [7]. Although differences exist in the experimental implementation of the various methods, all of them measure the local tip-sample contact stiffness. From the contact stiffness, the elastic properties of the sample can be determined using a contact-mechanics model. Thus all of these methods, as well as other contact AFM techniques, must deal with measurement challenges involving the conditions of nanoscale tip-sample contact.

The simplest contact-mechanics model to use in AFM-based techniques is the Hertzian model, which assumes a hemispherical tip shape and neglects adhesive forces [8,9]. The Hertzian model was successfully applied to systems with very low surface energy (very small adhesion forces) and small applied static loads (less than several nanonewton) [10]. These conditions prevented wear and plastic deformation of specially modified tips with hemispherical geometry. More detailed contact-mechanics models, such

*Corresponding author. Tel.: +1 303 497 4625; fax: +1 303 497 5030.
E-mail address: kopycins@boulder.nist.gov (M. Kopycinska-Müller).

0304-3991/$ - see front matter © 2006 Elsevier B.V. All rights reserved.
doi:10.1016/j.ultramic.2005.12.006

as the Derjaguin–Müller–Toporov (DMT) [11] and Johnson–Kendal–Roberts (JKR) models [12] have been adopted for AFM systems in cases where the adhesion forces could not be neglected [13,14]. However, even for the simplest model several parameters must be known, including the tip geometry and modulus, the applied static load, and the adhesive forces present (if any). The problem is that many of these parameters are neither easily measured nor well controlled. For instance, the static load F_C applied to the tip is usually calculated from the spring constant k_c and the deflection δ of the cantilever using Hooke's law for a spring: $F_C = k_c\delta$. However, determination of k_c requires separate measurements, and the values obtained sometimes differ by as much as 10–20% from those provided by the vendor [15]. Moreover, the force control in AFMs is not error-free, especially in instruments without closed-loop feedback. Finally, accurate characterization of the tip shape usually requires separate tip-reconstruction imaging experiments [16] or access to a scanning electron microscope (SEM) [17].

Determining local elastic properties with contact AFM-methods often requires higher static loads (several hundreds nanonewtons or larger) than those specified in Ref. [10]. For a material whose modulus is comparable to that of the tip (here, silicon), this ensures that the stress field created under the tip extends beyond a contamination layer. As a result, the tip shape changes with use, and the tip imaging or calibration procedures must be repeated frequently to ensure accurate measurements. Using commercially available coated tips does not prevent tip wear, because the coating is likely to fracture [18]. In addition, the effective elastic properties of such a tip are more complex due to the presence of the coating, which makes the determination of the local elastic modulus more complicated.

In spite of these difficulties, reliable quantitative elastic-property measurements using dynamic AFM techniques have been demonstrated, in particular using AFAM. AFAM uses a reference sample with known elastic modulus to calibrate the tip, an approach similar to that used in nanoindentation [19]. AFAM results for the indentation modulus M of various materials have been obtained that agreed with both nanoindentation results and literature values [20]. It has been found that the best agreement is obtained either by use of a reference sample with elastic properties similar to those of the unknown material or by use of two reference materials whose properties bracket those of the unknown sample [7]. We believe that such practices compensate in some way for the differences between the actual, nanoscale contact mechanics and that assumed by the theoretical models. Consequently, special care and attention must be paid to the choice of the AFAM reference sample. This requirement places limits on the ultimate applicability of AFAM to different materials.

In this paper, we describe experiments to improve our understanding of the nanoscale tip-sample contact conditions in AFAM or other contact AFM techniques. The main goal of our study is to understand how well the contact-mechanics models originally created for macroscopic scales can be used to evaluate the geometry of AFM tips on the nanoscale. To achieve this, we subjected several AFM tips to the same set of AFAM experiments. Information about the actual geometry of the tips was obtained through SEM imaging studies performed in parallel with the AFAM measurements. We analyzed the AFAM data using the Hertzian and DMT contact-mechanics models to obtain information about tip geometry. In our initial analysis, we assumed that if the measured contact stiffness increased as a function of static load, the tip possessed hemispherical geometry. The same, admittedly simplistic, approach was also used in a very recent study [21]. Our results show that the real tip-sample contact geometry is more complex than that assumed by the theoretical models. Using an approach that allowed for a nonideal tip geometry not only helped us to understand better the limitations of the current AFAM approach, but also showed us possible ways to improve it.

2. Principles of quantitative AFAM

Fig. 1 presents SEM images of a single-crystal silicon AFM cantilever typically used in AFAM experiments. Such a cantilever can be described as a beam with a trapezoidal cross-section that is constant throughout almost the entire length of the cantilever. The cantilever in Fig. 1 is about 240 μm long and 7 μm thick. The average width calculated from the base and the top of the trapezoid is about 35 μm. The cross-section of the cantilever changes rapidly over the last 20–25 μm of the length, resulting in a triangular end section. The tip is located between the rectangular and triangular parts of the cantilever.

In AFAM experiments, the resonant frequencies of the AFM cantilever are measured. Experimental methods for AFAM measurements are discussed in detail elsewhere [22,23]. First, the free-resonance frequencies are determined. After engaging the cantilever in contact with the sample surface, the so-called "contact-resonance" frequencies are then measured. The contact-resonance frequencies are greater than the corresponding free frequencies, due to interaction forces between the tip and the sample. An analytical model for the tip-sample system is used to extract information about the elastic properties from the contact-resonance frequencies. The system is modeled as a vibrating rectangular beam (AFM cantilever) that is clamped at one end and spring-coupled (interaction forces) to the sample surface by a tip located near the other end [24]. Additonal refinements to this model include lateral contact stiffness [25,26]. In preliminary data analysis, we found that for our experimental conditions, the values for the contact stiffness using a refined model did not differ significantly (typically $<1\%$) from the values obtained by the simple model. Furthermore, the functional dependence of k^* on F_C remained the same. Therefore, the final data

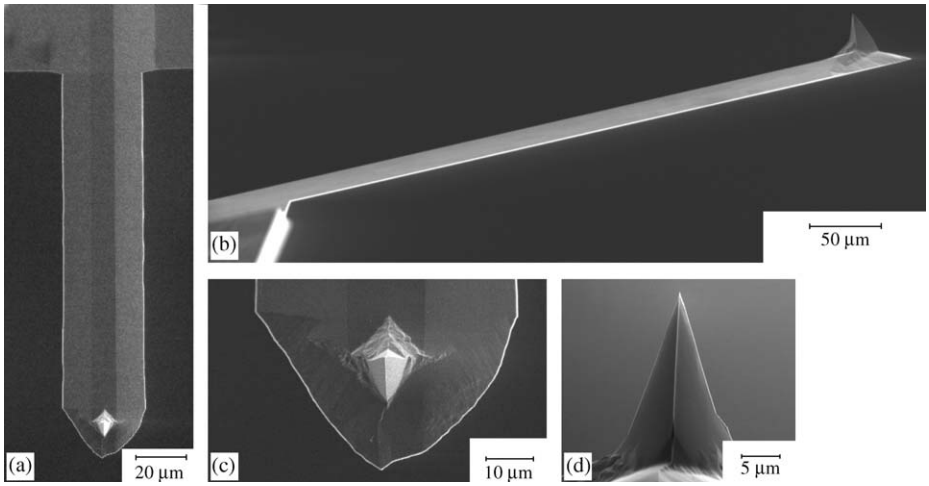

Fig. 1. SEM images of one of the AFM cantilevers used in this study. (a) Plan view and (b) side view images used to measure the cantilever dimensions. (c) Close-up of the region containing the tip. Note that the tip is not located at the exact end of the cantilever, and that the last 20–25 μm of the cantilever's length has a different geometry. (d) Side view of the AFM tip.

analysis was performed using the simpler model described above. The stiffness of the spring corresponds to the tip-sample contact stiffness k^*, which depends on the applied static load, the elastic properties of the tip and the sample, and the tip geometry. Therefore, experimental values of k^* can be used either to calculate the elastic modulus of a sample for a known tip geometry, or to characterize the tip geometry using a reference material with known elastic properties.

In AFAM measurements, values for the elastic modulus of an unknown sample are determined in relation to those of reference material. In this way, we can avoid direct characterization of the tip and the spring constant of the cantilever. To date, most AFAM studies have used the Hertzian contact model. For a hemispherical tip with radius R pressed against a flat surface with a static load F_C, the Hertzian contact stiffness k^*_H is given by

$$k^*_H = \sqrt[3]{6RF_C E^{*2}}, \tag{1}$$

where $E^* = (1/M_t + 1/M_s)^{-1}$ is the reduced Young's modulus, which depends on the indentation moduli M_t of the tip and M_s of the sample. In order to eliminate R and F_C from Eq. (1), values of k^*_r are determined for the reference (r) material and compared to values of k^*_s determined for the unknown sample (s). Assuming the same tip-sample contact conditions for both samples, Eq. (1) yields [22]:

$$E^*_s = E^*_r \left(\frac{k^*_s}{k^*_r}\right)^{3/2}. \tag{2}$$

Eq. (2) gives an upper limit for the elastic properties. The lower limit is calculated for a constant area (flat punch) geometry, in which the exponent $n = 3/2$ is replaced in Eq. (2) by $n = 1$ [22]. Values of the indentation modulus obtained with this procedure have been shown to agree closely with those obtained from the literature values and by nanoindentation. However, it has been found experimentally that unless the modulus M_r of the reference sample is similar to the modulus M_s of the unknown sample, the calculated values of M_s are either too low or too high [27]. In this study, we sought to understand this limitation by investigating the assumptions of the theoretical contact-mechanics models used in AFAM data analysis.

It should be noted that the Hertzian model neglects adhesion forces. In AFAM measurements, adhesion forces are generally $<10\%$ of the smallest applied static load (0.3–0.5 μN) and are therefore neglected. The DMT and JKR models include adhesion in the tip-sample interaction in two different ways. In the DMT model, the adhesion forces $F_{ad(DMT)}$ act outside the contact area. The resulting contact stiffness k^*_{DMT} is given by

$$k^*_{DMT} = \sqrt[3]{6R(F_C + F_{ad(DMT)})E^{*2}}. \tag{3}$$

The JKR model assumes that the adhesion forces $F_{ad(JKR)}$ act inside the contact area. The expression for the JKR contact stiffness $F_{ad(JKR)}$ has the following form [14]:

$$k^*_{JKR} = \sqrt[3]{24RF_{ad(JKR)}E^{*2}}\left(\frac{1+\sqrt{1+F_C/F_{ad(JKR)}}}{2}\right)^{2/3} \times \frac{1-\frac{1}{2}\left(\frac{1+\sqrt{1+F_C/F_{ad(JKR)}}}{2}\right)^{-1}}{1-\frac{1}{6}\left(\frac{1+\sqrt{1+F_C/F_{ad(JKR)}}}{2}\right)^{-1}}. \tag{4}$$

We used Eqs. (1), (3) and (4) to evaluate the effect of adhesion forces on k^* for a set of typical AFAM parameters: $R = 50$ nm, $E^* = 48.5$ GPa (a silicon tip in contact with a fused quartz sample), $F_{ad} = 0.08$ μN, and $F_C = 0.01-3$ μN. Including adhesion forces increased the

value of k^* in comparison to its value from the Hertzian model, especially for $F_C < 0.15\,\mu N$. For $F_C > 3\ F_{ad}$, k^*_{DMT} was always greater than k^*_H by $<10\%$ and decreased rapidly to $<2\%$ greater with increasing F_C. In addition, for typical AFAM experimental conditions there was virtually no difference between the DMT and JKR models. For $F_C > 0.6\,\mu N$, the values of k^* predicted by the two models differed by $<1\%$. Therefore, in our analysis of the AFAM data, we used only the DMT model due to its simpler mathematical expression.

3. Experimental procedures

3.1. Characterization of cantilever properties

In this study, we wanted to extract information about the tip radius of curvature R from experimental AFAM stiffness-load (k^* vs. F_C) data. One can use either Eq. (1) or (3) to calculate R, but these equations require the value of the applied static load F_C. Because we measure the cantilever deflection δ and $F_C = k_c\delta$, we therefore had to determine the cantilever spring constant k_c for each cantilever.

Ten different cantilevers were used in our experiments. The measured values of the first and second free-resonance frequencies f_1 and f_2 for all ten cantilevers are given in Table 1. We used the expression proposed by Sader *et al.* [28] to calculate k_c from the values of f_1 and the mass m of each cantilever:

$$k_c = 4\pi^2\kappa_S m f_1^2; \tag{5}$$

here $\kappa_S = 0.2427$ is the Sader constant. The mass m of a cantilever was calculated from the mass density of silicon ($\rho = 2.33\,kg/m^3$) [29] and the volume of the cantilever. The cantilever volume was calculated in the following way. From SEM images like those in Fig. 1 for four of the ten cantilevers, average values of the cantilever width W, the length L, and the thickness T were determined. The average values of L and T were used to predict the first free-resonance frequency of the cantilever using the relationship [25]

$$f_1 = 0.162\sqrt{\frac{E}{\rho}}\frac{T}{L^2}, \tag{6}$$

where E is the Young's modulus. For our silicon cantilevers, we use $E_{\langle 1\,1\,0\rangle} = 169\,GPa$ [29]. The average values of L and T were adjusted for each cantilever until the predicted value of f_1 from Eq. (6) matched the measured value in Table 1. For all of the cantilevers, we had to adjust L and T by less than 2–3% to obtain agreement.

The values of k_c obtained in this way are presented in Table 1. It can be seen that the values range from 35 to 41 N/m. The relative uniformity in the values of k_c is not surprising, considering that all the cantilevers were made of silicon, were provided by the same vendor, and had very similar dimensions. The values of f_1 and f_2, and thus the values of k_c, were used to segregate the cantilevers into three groups. For both groups I and II, all of the cantilevers in the group had very similar values of f_1 and f_2 and k_c. Group III is a miscellaneous group containing those cantilevers that did not fall into the other groups. In the text, we use these groups to refer not only to the cantilevers, but the tips attached to them as well.

Table 1
Characteristics of the cantilevers used in this study

Group	Cantilever	f_1 (kHz)	f_2 (kHz)	k_c (N/m)
I	*a*	161.56	1004.28	35
	b	161.55	1004.33	35
	c	161.06	1004.20	35
II	*a*	169.03	1049.00	40
	b	169.00	1048.40	40
	c	169.36	1056.06	40
	d	169.83	1055.31	40
III	*a*	171.25	1062.50	41
	b	164.21	1018.96	37
	c	167.30	1038.50	38

The measured values of the first and second free resonance frequencies f_1 and f_2 were used to divide the cantilevers into three groups. The estimated measurement uncertainty in frequency is ± 0.05 kHz The values of the spring constants k_c shown were calculated using the Sader expression [28].

3.2. AFAM/SEM studies

AFAM stiffness-load data were obtained with the ten cantilevers characterized in Table 1. For each cantilever, we measured the contact-resonance frequencies of the first and second bending modes as a function of the cantilever deflection δ. We used δ as the independent parameter instead of F_C because of the uncertainty connected with calculations of F_C from Hooke's law. All of the measurements were performed with the same sample of fused quartz. A value $M_{fq} = 68 \pm 2\,GPa$ for the indentation modulus of the fused quartz specimen was determined by nanoindentation. All of the cantilevers went through the same sequence of measurements, which contained seven separate measurement "tests". Each test comprised measurements at three to six different deflections. In the first test, $\delta = 10$, 20 and 30 nm. The next two tests consisted of measurements at four deflections increasing from 10 to 40 nm. In the fourth to seventh tests, δ was increased from 20 to 125 nm in six steps. This sequence of tests was chosen in order to investigate the behavior of new tips under varying conditions. Applying the same procedure to all of the cantilevers allowed us to compare changes occurring in the shapes of the tips. The tests were performed at different locations on the fused quartz sample.

SEM images were obtained for the new tips before engaging them in AFAM measurements. Through initial experiments, in which the tip was imaged after every

AFAM test, we learned that it was sufficient to acquire further SEM images for each tip only intermittently throughout the AFAM measurement sequence. For most of the tips, the SEM images were obtained after the first, third, fifth and seventh test. Each SEM session yielded four to five images of a tip at magnifications of 10^5 and 2×10^5. The SEM images were analyzed using commercial software to measure the radius of curvature R of each tip. With the software, a circle was drawn to fit the end of the tip as closely as possible. The radius of this circle was then taken as the value of R. Tips with a geometry markedly different from hemispherical were described as flat circular punches with respective radii a. For each image, two or three values of R were determined. This process yielded ten individual values of R that were averaged to obtain a single value. In the SEM images of small tips ($R < 50$ nm), it was often difficult to define the edges of the tip because the quality of the corresponding images was prone to vibrations and drift. In these cases, the accuracy of the measurement of R was limited. Because of these technical difficulties it was difficult to obtain tip images with magnifications higher than 2×10^5.

4. Results and discussion

4.1. Changes in tip shape occurring in AFAM measurements

Fig. 2 shows SEM images of three different new tips that represent the variety of geometries observed. Most of the tips were very sharp with a radius $R < 10$ nm, as shown in Fig. 2(a). These sharp tips broke during the AFAM measurements. The fracture events were observed in the AFAM data by a sudden, large increase in the contact stiffness. For each such event occurring in the AFAM data, the subsequent SEM images showed a change in tip shape consistent with fracture. Two of the new tips had initial radii of $R \approx 20-25$ nm, as shown in Fig. 2(b). We did not observe fracture of these tips during the AFAM tests, and the corresponding SEM images showed very little increase in R. The SEM image in Fig. 2(c) shows an extreme tip shape observed in our study. This tip was very blunt, even when new.

As mentioned above, the sharpest tips broke during the AFAM measurements. The images in Fig. 3 show some of the different tip geometries that resulted from fracture. Fig. 3(a) shows an SEM image obtained for tip Ic in Table 1. This tip broke during its second AFAM test at a static load of about 1 μN. The resulting geometry resembles a flat punch with radius $a \approx 20$ nm, rather than a hemisphere. There appears to be debris from the fracture on the right side of the tip. Tip IIIc, shown in Fig. 3(b), fractured twice during its fourth AFAM test at static loads of about 1.5 and 3 μN. The tip had a distinct plateau at its end with $a \approx 45$ nm. Tip Ib, shown in Fig. 3(c), fractured during its very first AFAM test at the static load of about 0.3 μN, but afterward remained approximately hemispherical, with $R \approx 20$ nm. Thus, there seems to be no rule

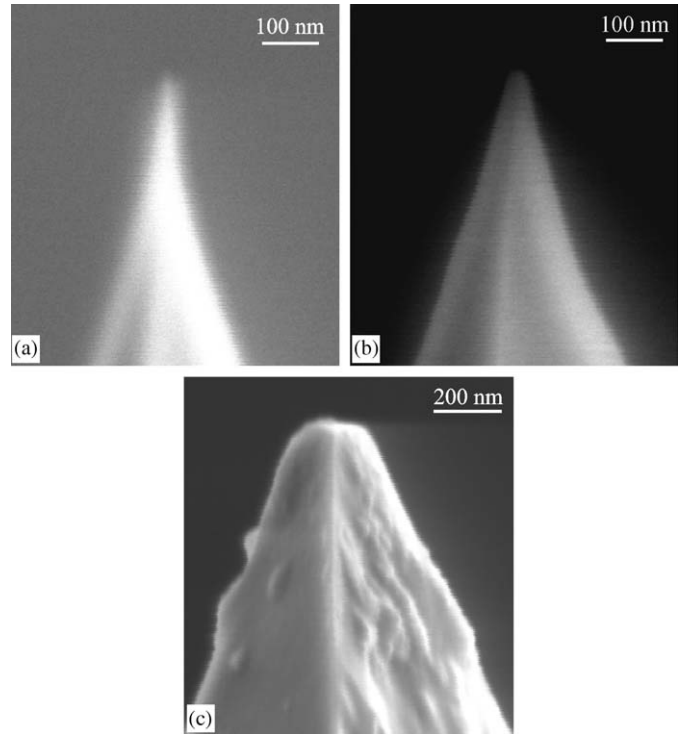

Fig. 2. SEM images of brand new tips revealing the wide differences in possible new-tip geometry. The scale is the same for all three images. (a) Sharp tip with radius of curvature $R < 10$ nm.(b) Tip with $R \sim 20$ nm. (c) Very blunt tip with possible surface contamination not seen in other tips.

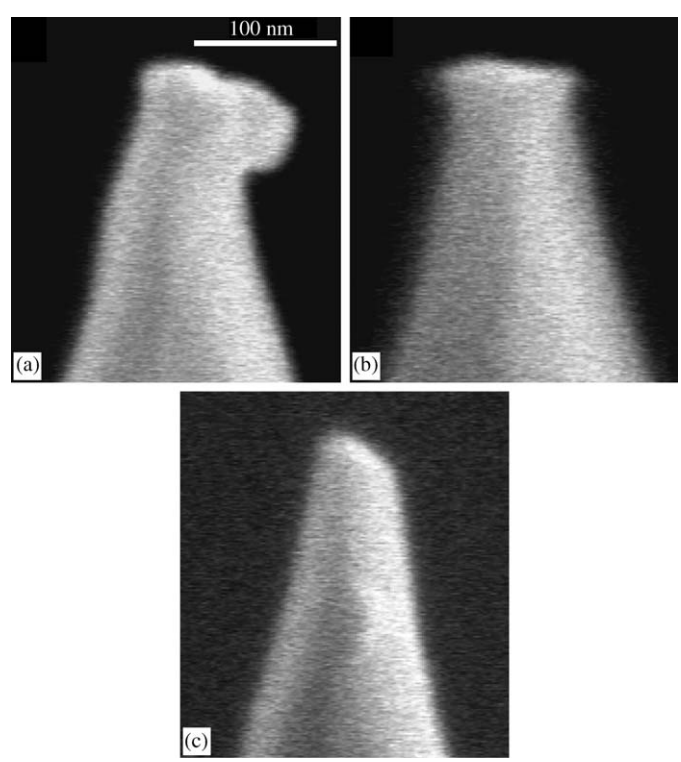

Fig. 3. SEM images of three tips affected by fracture in the AFAM measurements. The images were acquired after the (a) third, (b) fifth, and (c) first AFAM tests. The scale is the same for all three images.

concerning when a tip will break or what its shape will be after the fracture. This lack of consistency makes the analysis of AFAM data with simple contact-mechanics models even more complicated.

It is important to remember that the tip shape directly affects the values of k^* measured in AFAM experiments. We interpret AFAM data by use of contact-mechanics models that assume simple geometries, such as a sphere or flat punch to estimate lower and upper limits for the elastic modulus. However, as Figs. 2 and 3 reveal, the tip geometry is rarely simple and often changes with use. One such example is presented in Fig. 4. The new tip is very sharp with $R<10$ nm, as shown in Fig. 4(a). Values for the normalized contact stiffness k^*/k_c obtained with this tip from the AFAM tests are presented in Fig. 4(b). The legend of the plot defines the different symbols that correspond to different AFAM tests in which the applied static load was progressively increased, as described above. It can be seen that k^*/k_c was relatively low during the first test, as expected from Eq. (1) due to the small radius of the new tip. During the second and third test, the values of k^*/k_c increased slightly, suggesting a small increase in R. The values of k^*/k_c increased rapidly and significantly twice during the fourth AFAM test, suggesting two separate tip fracture events. In the subsequent tests, the values of k^*/k_c obtained for a given applied static load were very similar, indicating little, if any, further change in the tip shape. An image of the tip obtained at the end of the AFAM tests is shown in Fig. 4(c). It can be seen that the shape of the tip has indeed changed and now resembles a flat punch.

4.2. Analysis of AFAM data using contact-mechanics models

Eqs. (1) and (3) can be used to calculate the tip radius R from the AFAM data if the value of the applied static load F_C is known. The values of k_c in Table 1 allowed us to determine the values of F_C for each AFAM test. The values of R resulting from this contact-mechanics analysis of the AFAM data were then compared to the values obtained independently in the SEM images.

An example of this type of comparative analysis is shown in Fig. 5. Fig. 5(a) shows an SEM image obtained for tip IId when new. The tip possessed a hemispherical geometry in the SEM images and showed very little increase in R (20–25 nm) over the course of the AFAM measurements. The cantilever spring constant was 40 N/m. We used the Hertz and DMT contact-mechanics models to calculate R from the AFAM data. The values of R_H calculated using Eq. (1) are shown in Fig. 5(b). For the Hertzian model, we expect R_H to remain constant with no dependence on F_C. Instead, as can be seen in Fig. 5(b), R_H showed a strong dependence on F_C, decreasing from 90 to 18 nm as the static load increased from 0.4 to 5 μN.

Such behavior is not physically realistic and could be possibly explained by the presence of an offset stiffness (i.e., $k^* \neq 0$ for $F_C = 0$). An offset stiffness could result

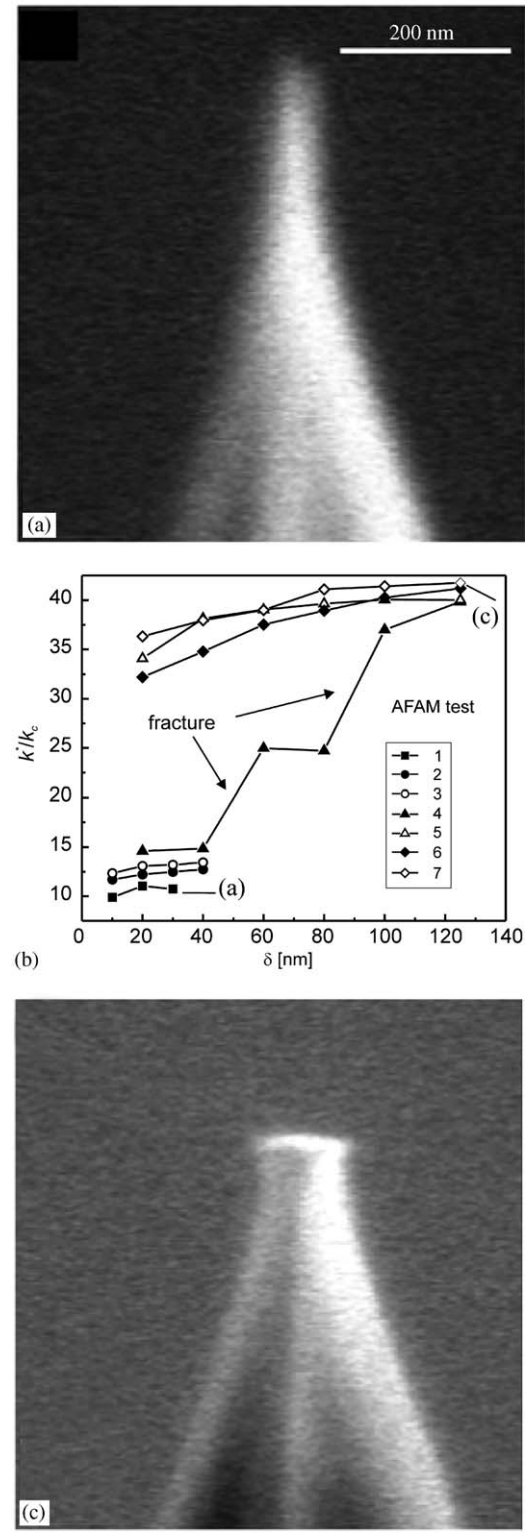

Fig. 4. Example of tip shape evolution in AFAM experiments. (a) SEM image of new tip IIIc. (b) Experimental AFAM values for the normalized contact stiffness k^*/k_c. The different symbols correspond to different AFAM tests in which the load was progressively increased. Indicated are the points at which the SEM images of the tip in (a) and (c) were acquired. The arrows indicate tip fracture events. (c) SEM image of the same tip after performing the set of AFAM tests. The scale is the same as in (a).

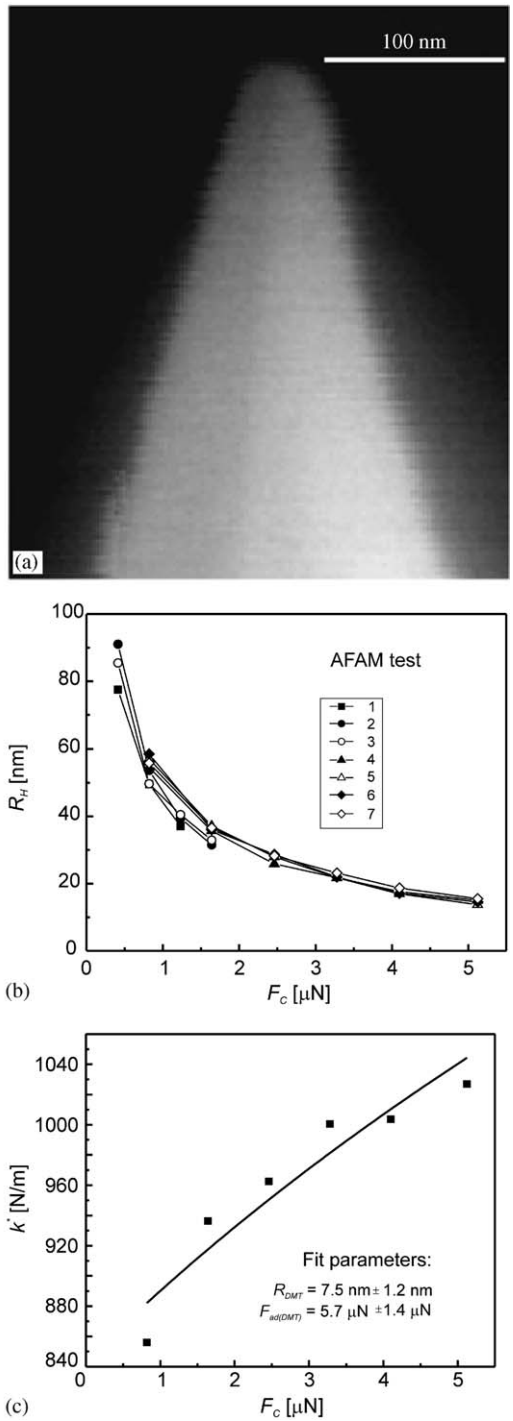

Fig. 5. (a) SEM image of new tip IId. (b) Tip radius R_H versus applied static load F_C calculated using the Hertzian contact model. (c) Comparison between experimental values for k^* (points) and those predicted using the DMT contact-mechanics model as defined in Eq. (3) (line). The values for R and F_{ad} used as fit parameters are given.

from either the presence of an adhesion force F_{ad} or from a geometry different from a hemisphere. To examine the issue of adhesion forces, we used the DMT model to analyze the experimental values of k^*_{AFAM} obtained with tip IId. We used Eq. (3) to fit the experimental dependence of k^*_{AFAM} on F_C using R_{DMT} and $F_{ad(DMT)}$ as fit parameters.

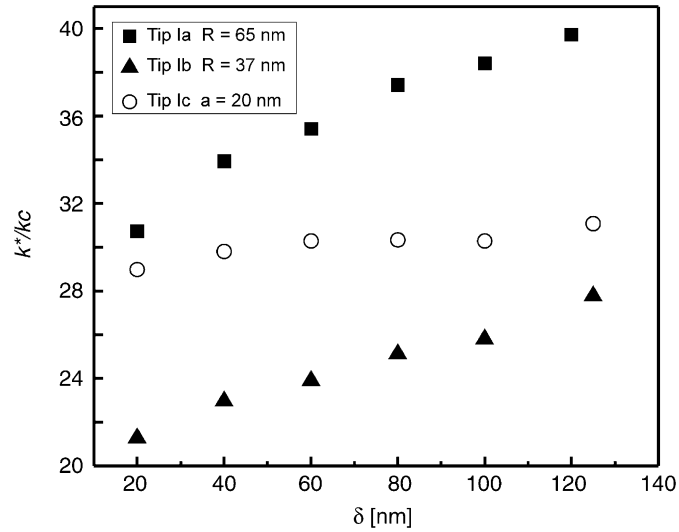

Fig. 6. Normalized contact stiffness k^*/k_c as a function of cantilever deflection δ. The three sets of data were obtained with three different tips attached to cantilevers with nearly identical values of their spring constants k_c. The differences in the values of k^*/k_c were caused by the differences in tip geometry.

We used commercial software to perform fitting and to calculate the corresponding error values. As seen in Fig. 5(c), the dependence of k^* on F_C predicted by the DMT model agreed with our data reasonably well. However, the values for R_{DMT} and $F_{ad(DMT)}$ needed to match the data differed strongly from the actual values. The best-fit value of R_{DMT} was about 8 nm, whereas the SEM images yielded values from 20 to 25 nm for the new and used tip. The value for the adhesion force $F_{ad(DMT)}$ determined by the fitting procedure was very large—almost 6 μN. This value is much larger than the estimated maximum applied static force (4–6 μN) for any of the AFAM measurements. Furthermore, the expected values for F_{ad} are ~0.1 μN, as estimated from the pull-off forces observed during AFAM measurements. We analyzed the AFAM and SEM data for the other nine tips in a similar manner. Results very similar to those in Figs. 5(b) and (c) were obtained. For all of the tips, the values calculated for R_H using the Hertzian approach showed a dependence on F_C. Analysis with the DMT yielded values for R_{DMT} that differed significantly, but not systematically, from the values obtained from the SEM images, while the values of $F_{ad(DMT)}$ were always 10–100 times larger than expected. The results of this analysis indicated that the assumptions of the Hertzian and DMT models did not describe the tip-sample contact geometry accurately.

In our analysis, we used the values for k_c given in Table 1, treating k_c as a known parameter. However, we were aware that our calculations of the spring constant had an uncertainty resulting from discrepancies between the real and the assumed rectangular beam. Therefore, the AFAM data were re-analyzed using k_c as an additional

fitting parameter. We found that we could describe the AFAM data with the DMT model using values for R_{DMT} and $F_{ad(DMT)}$ that agreed reasonably well with the expected values. However, the results obtained for the same tip from test to test were not consistent. The values of k_c were not constant (for tip Ia, k_c ranged from 30 to 50 N/m), which is not physically realistic. Furthermore, sometimes the values of R_{DMT} decreased with use, while the SEM data showed an increase.

Finally, we observed that the function $k^*(F_C)$ depends on the tip geometry. Fig. 6 presents data obtained with the three cantilevers from group I. The cantilevers had very similar values of their first and second free-resonance frequencies, and therefore had virtually the same values of their spring constants k_c. In Fig. 6, the values of the normalized contact stiffness k^*/k_c are plotted as a function of the cantilever deflection to obtain a plot independent of k_c. SEM images indicated that tips Ia and Ib could be described as hemispherical with $R = 65$ and 37 nm, respectively. The shape of tip Ic, shown in Fig. 3(a), was much closer to that of a flat punch than that of a sphere. As can be seen in Fig. 6, the dependence of k^*/k_c on the cantilever deflection δ reflects these differences in tip geometry. The values of k^*/k_c determined for tips Ia and Ib increased significantly with the cantilever deflection and the slopes of the normalized stiffness-load curves were similar. In addition, values of k^*/k_c determined with tip Ia are greater than these determined with tip Ib. These two facts agree well with the available SEM information. The results obtained with tip Ic show different behavior. The values of k^*/k_c increase little with the increasing δ, indicating a geometry close to that of a flat punch. This is also consistent with the corresponding SEM image.

We found a qualitative correlation between the slope of the AFAM stiffness-load data and the SEM geometry information, in that k^* increased with F_C for approximately hemispherical tips and stayed relatively constant with F_C for flat-punch type tips. However, we have already shown that quantitative data analysis using a simple tip geometry cannot be made. Therefore, we have followed ideas used in nanoindentation that allow for non-ideal tip shapes. In nanoindentation, the values of the contact stiffness are determined from the slope of the unloading part of the *load–displacement* curve. The unloading curve is fitted using a power law [19]. It was found that the exponent varies from 1.25 for a flat punch to 1.5 for a sphere. In AFAM measurements, we obtain a *stiffness–load* curve that can also be described with a power law:

$$k^* = \beta F_C^n, \tag{7}$$

where β is a factor depending on the tip geometry and the elastic properties of the tip and the sample. As defined in Eq. (7), n varies from 0 for a flat punch to 1/3 for a hemisphere. We used Eq. (7) to fit the AFAM data presented in Fig. 6. The values of n obtained for tips Ia and Ib were 0.140 and 0.142, respectively. This result indicates that the two tips had nearly the same geometry, which was between that of a hemisphere and that of a flat punch. The exponent factor n determined for tip Ic was 0.03, which is very close to that expected for flat-punch geometry.

The results of this quantitative analysis of AFAM data suggest that contact geometry occurring on a very small scale of tens of nanometers cannot be idealized. It should be noted that in typical AFAM measurements, the estimated diameter of the contact area and the tip-sample deformation are less than 40 and 5 nm, respectively. This means that the tip shape must be characterized on exactly the same scale. However, the SEM images lacked the necessary spatial resolution to obtain such information at the very last nanometers of the tip. This explains why AFAM data obtained with tips that appeared hemispherical in SEM images could not be evaluated using a power-law function with $n = 1/3$.

5. Summary and conclusions

We have performed a series of defined atomic force acoustic microscopy (AFAM) measurements with ten different atomic force microscope (AFM) tips in order to study the impact of tip geometry on the quantitative analysis of contact stiffness data. Information about the tip geometry during the AFAM measurements was obtained from high-resolution scanning electron microscope (SEM) images. We found that commercially obtained AFM tips had various geometries even when new, although the majority of tips were very sharp ($R < 10$ nm). Such sharp tips always broke at some point in the AFAM measurements. The fracture events were easy to identify during the AFAM experiments by a sudden increase in the measured values of the contact-resonance frequencies. After fracture, the tip radius increased gradually with use. However, despite applying relatively high loads ($F_C > 3$ μN), the radius of most tips stayed below 70 nm. This ensures the high lateral spatial resolution of AFAM.

Efforts to apply basic contact-mechanics models were unsuccessful, even for tips showing a hemispherical geometry in the SEM images. Calculations of the tip radius using the Hertzian model showed a strong dependence on the applied static load, which is not physically realistic. Applying the Derjaguin–Müller–Toporov (DMT) contact-mechanics model was not successful either. The values determined for R varied indeterminately from the SEM results, and the values obtained for the adhesion forces were higher than the highest load applied in our measurements (few μN). We analyzed our data successfully using an approach adopted from nanoindentation, in which the AFAM stiffness-load data were described by a power law with an exponent n dependent on the tip geometry. This analysis showed that n was characteristic of tip geometries intermediate between flat punch and hemisphere. In many contact AFM techniques, the tip-sample contact occurs on the scale of a few nanometers. SEM images typically lacked the resolution needed to sufficiently characterize tip geometry

on this scale. Therefore, the approach of nonideal geometry characterization shows promise towards improving the quantitative analysis of data obtained with AFAM and other contact AFM techniques.

Acknowledgments

We thank U. Rabe (IZFP, Saarbrücken, Germany) for valuable discussions.

References

[1] Q. Zhong, D. Inniss, K. Kjoller, V.B. Elings, Surf. Sci. 280 (1993) L688.
[2] J.P. Cleveland, B. Anczykowski, A.E. Schmid, V.B. Elings, Appl. Phys. Lett. 72 (1998) 2613.
[3] J. Tamayo, R. Garcia, Appl. Phys. Lett. 73 (1998) 2926.
[4] R.E. Geer, O.V. Kolosov, G.A.D. Briggs, G.S. Shekhawat, J. Appl. Phys. 91 (2002) 4549.
[5] M.T. Cuberes, H.E. Assender, G.A.D. Briggs, O.L. Kolosov, J. Phys. D: Appl. Phys. 33 (2000) 2347.
[6] K. Yamanaka, Y. Maruyama, T. Tsuji, K. Nakamoto, Appl. Phys. Lett. 78 (2001) 1939.
[7] U. Rabe, M. Kopycinska, S. Hirsekorn, J. Muñoz Saldaña, G.A. Schneider, W. Arnold, J. Phys. D: Appl. Phys. 35 (2002) 2621.
[8] K.L. Johnson, in: Contact Mechanics, Cambridge University Press, Cambridge, 1985, pp. 90–106.
[9] F. Stahl, B. Cretin, in: J.P. Jones (Ed.), Acoustical Imaging, vol. 21, Plenum, New York, 1995, pp. 305–311.
[10] U.D. Schwarz, O. Zwörner, P. Köster, R. Wiesendanger, Phys. Rev. B 56 (1997) 6987.
[11] B.V. Derjaguin, V.M. Muller, Yu.P. Toporov, J. Colloid Interf. Sci. 53 (1975) 314.
[12] K.L. Johnson, K. Kendall, A.D. Roberts, Proc. R. Soc. Lond. A 324 (1971) 301.
[13] R.W. Carpick, D.F. Ogletree, M. Salmeron, J. Coll. Interf. Sci. 211 (1999) 395.
[14] O. Piétrement, M. Troyon, J. Coll. Inter. Sci. 226 (2000) 166.
[15] C.T. Gibson, D.A. Smith, C.J. Roberts, Nanotechnology 16 (2005) 234.
[16] L.S. Dongmo, J.S. Villarubia, S.N. Jones, T.B. Renegar, M.T. Postek, J.F. Song, Ultramicroscopy 85 (2000) 141.
[17] M. Kopycinska-Müller, R.H. Geiss, P. Rice, D.C. Hurley, in: S.V. Kalinin, B. Goldberg, L.M. Eng, B.D. Huey (Eds.), Scanning-probe and other novel microscopies of local phenomena in nanostructured materials, Materials Research Symposium Proceedings 838E. Warrendale, PA, electronic only publication, O-10.16.
[18] S. Amelio, A.V. Goldade, U. Rabe, V. Scherer, B. Bhushan, W. Arnold, Thin Solid Films 392 (2001) 75.
[19] W.C. Oliver, G.M. Pharr, J. Mater. Res. 7 (1992) 1564.
[20] D.C. Hurley, M. Kopycinska-Müller, A.B. Kos, R.H. Geiss, Adv. Eng. Mater. 7 (2005) 713.
[21] D. Passerii, A. Bettucci, M. Germano, M. Rossi, A. Alipi, S. Orlanducci, M.L. Terranova, M. Ciavarella, Rev. Sci. Instrum. 76 (2005) 093904.
[22] U. Rabe, S. Amelio, M. Kopycinska, S. Hirsekorn, M. Kempf, M. Göcken, W. Arnold, Surf. Interf. Anal. 33 (2002) 65.
[23] D.C. Hurley, K. Shen, N.M. Jennett, J.A. Turner, J. Appl. Phys. 94 (2003) 2347.
[24] U. Rabe, K. Janser, W. Arnold, Rev. Sci. Instrum. 67 (1996) 3281.
[25] U. Rabe, J.A. Turner, W. Arnold, Appl. Phys. A 66 (1998) S277.
[26] E. Dupas, G. Gremaud, A. Kulik, J.-L. Loubet, Rev. Sci. Instrum. 72 (2001) 3891.
[27] M. Kopycinska-Müller, On the elastic properties of nanocrystalline materials and the determination of elastic properties on nanoscale using the atomic force acoustic microscopy technique, Ph.D. thesis, University of Saarland, Saarbrücken, Germany, 2005.
[28] J.E. Sader, I. Larson, P. Mulvaney, L.R. White, Rev. Sci. Instrum. 66 (1995) 3789.
[29] G. Simmons, H. Wang, in: Single crystal elastic constants and calculated aggregate properties: A handbook, The MIT Press, Cambridge, 1971, p. 85.